Received: 17 April 2024 | Revised: 10 July 2024 | Accepted: 18 July 2024

DOI: 10.1002/pamm.202400012

RESEARCH ARTICLE

Microscale modeling of damage mechanisms in dual-phase steel DP800

Alexander Niehüser | **Jörn Mosler**

Institute of Mechanics, TU Dortmund University, Dortmund, Germany

Correspondence
Alexander Niehüser, Institute of Mechanics, TU Dortmund University, Dortmund, Germany.
Email: alexander.niehueser@tu-dortmund.de

Funding information
Deutsche Forschungsgemeinschaft, Grant/Award Number: 278868966

Abstract

Dual-phase steels are very popular in the automotive industry due to their high strength while maintaining good formability. The macroscopic formability of this polycrystalline material is governed by deformations and damage mechanisms at the microscale. To describe the mechanical properties associated with these mechanisms, a crystal plasticity theory is coupled with interface models and integrated into representative volume elements (RVEs) of DP800 in a thermodynamically consistent manner. The interface models capture decohesion at the grain boundaries via a cohesive interface model as well as the initiation and propagation of micro-cracks (damage) within the quasi-brittle martensite phase via a phase-field approach. In this contribution, the focus lies on the conceptual framework combining above models in a finite element setting. Furthermore, the interaction and activation of the different (damage) mechanisms will be shown in order to highlight the predictive capabilities of the presented framework.

1 | INTRODUCTION

Dual-phase (DP) steels have already been subject of active research and industrial applications over many decades. In general, the soft ferrite phase allows for a low initial yield stress whereas the martensite phase provides a high ultimate tensile strength, which makes DP steels perfectly suitable for sheet-forming operations [1]. In these forming processes, DP steels are subject to severe plastic deformations, which lead to damage in the form of void nucleation, growth, and coalescence in the microstructure which, in turn, results in degradation of mechanical properties and ultimately in failure. Therefore, understanding and quantifying the damage behavior is crucial in order to optimize the processes and increase the performance as well as the reliability of final parts and structures [2].

Although understanding the damage mechanism and their effect on the macroscopic mechanical properties is still an ongoing field of research [3], experiments reveal that the fundamental damage mechanisms of DP steels are (1) ferrite grain boundary decohesion, (2) martensite/ferrite (MF) interface decohesion, and (3) cracking of the quasi-brittle martensite phases. Furthermore, these main mechanisms may be accompanied by cracking or decohesion of nonmetallic inclusions or precipitates [2].

The main goal of this contribution is to model those main (damage) mechanisms at the microscale in a thermodynamically consistent manner. The first mechanism to take into account is large plastic deformation within the BCC crystal structure of the ferrite grains. Therefore, a rate-independent crystal plasticity formulation is employed. To overcome the

problems related to the computation of non-unique slips on those crystallographic slip systems [4], a popular ansatz based on an augmented Lagrangian approach [5] is utilized. This approach regularizes the problem via a pseudo-viscosity but does not introduce an undesired physical viscosity—as penalty approaches do. With that at hand, the effect of grain size distributions and crystal orientations may be studied.

Next, a cohesive zone model [6, 7] is employed to capture grain boundary decohesion at martensite/ferrite (MF) and ferrite/ferrite (FF) interfaces. The interfaces have an initial thickness of zero. Once a critical stress value is reached, damage is initiated, which leads to opening of the interfaces, that is, void nucleation. These voids may then further grow or coalesce with other voids.

In contrast to grain boundary decohesion, the location of crack initiation and the crack path in the quasi-brittle martensite are not known beforehand. Therefore, a Griffith-type phase-field model for brittle fracture [8, 9] is adopted. The resulting two-field problem is solved by alternate minimization. Based thereon, the model is capable of predicting arbitrary crack paths within the martensite phases.

In summary, the following modeling approaches will be employed to capture above-mentioned (damage) mechanisms:

- Crystal plasticity model to account for large plastic deformations within ferrite grains.
- Cohesive interface model to capture grain boundary decohesion at martensite/ferrite and ferrite/ferrite interfaces.
- Phase-field model to capture crack initiation and propagation of the quasi-brittle martensitic phase.

Moreover, the focus lies on the conceptual framework combining the models in a finite element setting and showcasing the interaction of those mechanisms via RVEs of the microstructure of a DP800.

2 | CONSTITUTIVE RELATIONS

This section addresses the constitutive relations employed in the current contribution. First, the crystal plasticity model is presented in Section 2.1 in order to account for plastic deformations within the ferrite matrix. Next, the damage mechanisms of grain boundary decohesion are modeled by cohesive interfaces in Section 2.2. Finally, the cracking of the quasi-brittle martensite is modeled by a phase-field approach as presented in Section 2.3. Due to the large deformations observed at the micro-scale within the polycrystal, a finite deformation setting is chosen where the deformation gradient is denoted $\boldsymbol{F} := \mathrm{GRAD}\,\boldsymbol{\varphi} = \partial \boldsymbol{x}/\partial \boldsymbol{X}$.

2.1 | Crystal plasticity model

In order to account for plastic deformations and the crystal structure of the ferrite, the deformation gradient is multiplicatively decomposed into an elastic and plastic part $\boldsymbol{F} = \boldsymbol{F}^{\mathrm{e}} \cdot \boldsymbol{F}^{\mathrm{p}}$, where the plastic part $\boldsymbol{F}^{\mathrm{p}}$ describes the irreversible dislocation movement on crystallographic slip systems. The mechanical response is then assumed to be governed by the additive decomposition of the volume-specific Helmholtz free energy density function into an elastic and plastic part $\Psi = \Psi^{\mathrm{e}}(\boldsymbol{F}^{\mathrm{e}}) + \Psi^{p}(\gamma^{\alpha})$. The elastic behavior is modeled by the compressible isotropic neo-Hookean type free energy

$$\Psi^{\mathrm{e}} = \frac{1}{2}\kappa \log^2(J^{\mathrm{e}}) + \frac{1}{2} G \left[\mathrm{tr}(\bar{\boldsymbol{C}}^{\mathrm{e}}) - 3\right] \tag{1}$$

with $\bar{\boldsymbol{C}}^{\mathrm{e}} = J^{\mathrm{e}-2/3}\, \boldsymbol{F}^{\mathrm{e}T} \cdot \boldsymbol{F}^{\mathrm{e}}$, bulk modulus κ, and shear modulus G. The plastic behavior is modeled by a Taylor-type potential depending on the cumulative inelastic slips A of the crystal

$$\Psi^{\mathrm{p}}(A) = \Delta Q \left(A + \frac{1}{p}(\exp(-p\,A) - 1) \right) \qquad \text{with } A := \sum_{\alpha=1}^{n_{\mathrm{sys}}} \gamma^{\alpha}. \tag{2}$$

Here, variable γ^{α} poses the inelastic slip on each individual slip system α, ΔQ is a hardening parameter, and p a shape parameter. Clearly, other hardening laws also accounting for latent hardening or dislocation densities may be included easily, but are not the focus of this contribution. Applying standard Colemann and Noll procedure [10] to the isothermal

Clausius–Planck–inequality $\mathscr{D} = \boldsymbol{P} : \dot{\boldsymbol{F}} - \dot{\Psi} \geq 0$ yields the first Piola–Kirchhoff stress tensor

$$\boldsymbol{P} = \frac{\partial \Psi^{\mathrm{e}}}{\partial \boldsymbol{F}^{\mathrm{e}}} \cdot \boldsymbol{F}^{\mathrm{p-T}} = \boldsymbol{F}^{\mathrm{e-T}} \cdot \boldsymbol{\Sigma} \cdot \boldsymbol{F}^{\mathrm{p-T}} \tag{3}$$

and the reduced Dissipation inequality

$$\mathscr{D} = \boldsymbol{\Sigma} : \boldsymbol{L}^{\mathrm{p}} + \sum_{\alpha=1}^{n_{\mathrm{sys}}} Q^{\alpha} \dot{\gamma}^{\alpha} \geq 0. \tag{4}$$

where $\boldsymbol{\Sigma} = \boldsymbol{F}^{\mathrm{eT}} \cdot \partial_{\boldsymbol{F}^{\mathrm{e}}} \Psi^{\mathrm{e}}$ denotes the Mandel stress tensor, $\boldsymbol{L}^{\mathrm{p}} = \dot{\boldsymbol{F}}^{\mathrm{p}} \cdot \boldsymbol{F}^{\mathrm{p-1}}$ the plastic velocity gradient, and $Q^{\alpha} = -\partial_{\gamma^{\alpha}} \Psi^{\mathrm{p}}$ the work conjugated driving force to γ^{α}. To complete the model, the yield functions for each slip system $\alpha \in \{1, \dots, n_{\mathrm{sys}}\}$ based on Schmid's law [4] are defined as

$$\Phi^{\alpha} = |\boldsymbol{\Sigma} : \boldsymbol{M}^{\alpha}| - \left[Q_0^{\alpha} - Q^{\alpha}\right] \leq 0, \tag{5}$$

where $\boldsymbol{M}^{\alpha} = \boldsymbol{S}^{\alpha} \otimes \boldsymbol{N}^{\alpha}$ is the deviatoric slip system tensor consisting of the normal vectors of the slip planes $\boldsymbol{N}^{\alpha}$ and the slip directions $\boldsymbol{S}^{\alpha}$. Q_0^{α} denotes the initial yield limit of each slip system. The required evolution equations for $\boldsymbol{F}^{\mathrm{p}}$ and γ^{α} may then be derived from the postulate of maximum dissipation

$$\begin{aligned} \max_{(\boldsymbol{\Sigma}, Q^{\alpha})} \quad & \mathscr{D} = \boldsymbol{\Sigma} : \boldsymbol{L}^{\mathrm{p}} + \sum_{\alpha=1}^{n_{\mathrm{sys}}} Q^{\alpha} \dot{\gamma}^{\alpha} \geq 0 \\ \text{s.t.} \quad & \Phi^{\alpha}(\boldsymbol{\Sigma}, Q^{\alpha}) \leq 0 \quad \forall \alpha \in \{1, \dots, n_{\mathrm{sys}}\}. \end{aligned} \tag{6}$$

Unfortunately, this optimization problem faces at least two problems in the case of rate-independent crystal plasticity: (1) determination of active slip systems and (2) computation of non-unique slips on those crystallographic slip systems [4, 11]. Therefore, a popular ansatz based on the augmented Lagrangian [5] is employed where the inequality constraints (yield functions) are incorporated into the reduced Lagrangian

$$\mathscr{L}(\boldsymbol{\Sigma}, Q^{\alpha}, \dot{\lambda}^{\alpha}) = -\mathscr{D}(\boldsymbol{\Sigma}, Q^{\alpha}) + \frac{1}{2\,\mu} \sum_{\alpha=1}^{n_{\mathrm{sys}}} \left[\max[0, \dot{\lambda}^{\alpha} + \mu\, \Phi^{\alpha}(\boldsymbol{\Sigma}, Q^{\alpha})]^2 - (\dot{\lambda}^{\alpha})^2\right]. \tag{7}$$

Here, the penalty-parameter μ naturally deals with selecting the active slip systems and the Lagrange multipliers $\dot{\lambda}^{\alpha}$ enforce the exact fulfillment of the yield conditions Φ^{α}. Demanding stationarity of this functional, applying a time-discretization scheme to the evolution equations and employing a fixed-point update scheme results in the discretized nonlinear system of equations to be solved

$$R^{\alpha}(\Delta\lambda^{\beta}_{(i+1)}) = \Delta\lambda^{\alpha}_{(i+1)} - \max[0, \Delta\lambda^{\alpha}_{(i)} + \Delta t\, \mu_{(i)}\, \Phi^{\alpha}(\boldsymbol{C}, \Delta\lambda^{\beta}_{(i+1)})] \tag{8}$$

These equations are solved by means of a Newton scheme where the penalty-parameter $\mu_{(i)}$ is successively increased in an outer loop. Details on the implementation and the algorithm are given in Refs. [5, 12].

2.2 | Grain boundary decohesion—cohesive interfaces

Next, an isotropic cohesive interface model including damage based on Refs. [6, 7] is presented, which will be used to capture grain boundary decohesion at FF and MF interfaces. In order to define the balance laws and constitutive equations, the body Ω is considered to be separated during deformation into the two parts Ω^- and Ω^+ by means of an internal surface $\partial_s\Omega$, that is, $\Omega = \Omega^- \cup \Omega^+ \cup \partial_s\Omega$. This internal surface has zero-thickness in the undeformed configuration but may open in the deformed configuration leading to discontinuous displacements across the interface, denoted as the displacement jump $[\![\boldsymbol{u}]\!] = \boldsymbol{u}^+ - \boldsymbol{u}^-$, where $\boldsymbol{u}^+$ and $\boldsymbol{u}^-$ are the displacements of two initially coinciding points in Ω^+ and

Ω^-. By introducing $\boldsymbol{T}$ as the traction vector of the interface in the reference configuration, the balance of linear momentum at the interface for isotropic models in local form [13] reads

$$\boldsymbol{T}^+ + \boldsymbol{T}^- = \boldsymbol{0}, \tag{9}$$

where $\boldsymbol{T}^+$ and $\boldsymbol{T}^-$ are the traction vectors of the respective lower and upper surface of the interface. This balance equation basically requires traction continuity across the interface, that is, $[\![\boldsymbol{T}]\!] = 0$. A detailed discussion about the continuity of the traction vector across the interface can be found in Javili et al. [14].

In order to fulfill balance of angular momentum for isotropic models, the displacement jump $[\![\boldsymbol{u}]\!]$ has to be collinear to the traction vector $\boldsymbol{T}$, that is, $\boldsymbol{T} \,||\, [\![\boldsymbol{u}]\!]$, as shown in Heitbreder et al. [7]. Therefore, the model can be interpreted as springs or fibers connecting the two surfaces of a bulk. A consistent extension for the anisotropic case of generalized imperfect interfaces fulfilling all fundamental balance laws is discussed in Refs. [6, 13]. Nevertheless, in this contribution, only isotropic cohesive zone models including damage shall be considered. To be more specific, the Helmholtz energy is chosen as

$$\Psi([\![\boldsymbol{u}]\!], d) = [1-d]\,\Psi^e = [1-d]\,\frac{1}{2}\,\tilde{E}\,[\![\boldsymbol{u}]\!]\cdot[\![\boldsymbol{u}]\!] \tag{10}$$

with the damage variable d and the interface (numerical) stiffness $\tilde{E}$. Based on this potential, the traction vector can be derived as

$$\boldsymbol{T} = \frac{\partial \Psi}{\partial [\![\boldsymbol{u}]\!]} = [1-d]\,\tilde{E}\,[\![\boldsymbol{u}]\!], \tag{11}$$

which is known as the traction separation law. Thus, collinearity is obviously fulfilled. To complete the model and fulfill thermodynamic consistency, a suitable evolution law for the damage variable is required, that is, $\dot{d} \geq 0$. Therefore, a monotonically increasing variable α is introduced as $\alpha_{n+1} = \max(\alpha_n, \Psi_{n+1})$ with $\alpha(t=0) = \alpha_0 = Q_0^2/(2\tilde{E})$. The damage evolution itself is then based on an exponential ansatz [7]

$$d(\alpha) = 1 - \sqrt{\frac{\alpha_0}{\alpha}}\,\exp\left(-[\sqrt{\alpha} - \sqrt{\alpha_0}]\,\frac{Q_0}{\sqrt{\frac{1}{2}\,\tilde{E}\,\mathcal{G}_f}}\right) \tag{12}$$

ensuring boundedness between 0 (=pristine material) and 1 (=failed/cracked material) and damage initiation when the critical stress Q_0 of the interfaces is reached. Here, $\mathcal{G}_f$ is the fracture energy.

One final but important aspect to consider is the mechanical response under compression. The current traction separation law (11) would allow self-penetration, which is unphysical. Therefore, the initial stiffness of the interface is recovered in the compressive regime yielding the modified traction separation law

$$\boldsymbol{T} = \begin{cases} [1-d]\,\tilde{E}\,[\![\boldsymbol{u}]\!] & \text{if } [\![\boldsymbol{u}]\!]\cdot\boldsymbol{n} \geq 0 \\ \tilde{E}\,[\![\boldsymbol{u}]\!] & \text{if } [\![\boldsymbol{u}]\!]\cdot\boldsymbol{n} < 0 \end{cases} \tag{13}$$

where $\boldsymbol{n}$ is the normal vector of the interface. In order to account for different properties of FF and MF interfaces, different sets of material parameters $(\tilde{E}, Q_0, \mathcal{G}_f)$ may be chosen.

2.3 | Martensite cracking—phase-field model

Unlike in the case of grain boundary decohesion, the location of crack initiation and the crack path in the quasi-brittle martensite are not known beforehand. Therefore, a Griffith-type phase-field model for brittle fracture based on Refs. [8, 9] is adopted. Following Miehe et al. [9], the corresponding time-discrete minimization problem of the incremental

variational potential reads

$$(\boldsymbol{u}, d) = \underset{(\boldsymbol{u},d)}{\operatorname{argmin}} \left\{ \int_\Omega \left[\Psi(\boldsymbol{u}, d) + g_c\, \gamma(d, \nabla d) + \frac{1}{2}\, \eta \left(\frac{\Delta d}{\Delta t} \right)^2 \right] \mathrm{d}V - P(\boldsymbol{u}) \mid d - d_n \geq 0 \right\} \tag{14}$$

with the crack surface density function

$$\gamma(d, \nabla d) = \frac{1}{2\,l}\, d^2 + \frac{l}{2}\, |\nabla d|^2. \tag{15}$$

Here, g_c is the Griffith-type critical energy release rate, l is the length scale parameter, and η is a viscous regularization parameter to stabilize the numerical treatment. In order to capture the micro-crack closure reopening (MCR) effect, the Helmholtz energy is decomposed into a plus part (tension/shear) that may damage and a minus part (compression) that may not damage based on the volumetric–deviatoric split of the deformation gradient

$$\Psi(\boldsymbol{F}, d) = [(1-d)^2 + k]\, \Psi_0^+(\boldsymbol{F}) + \Psi_0^-(\boldsymbol{F}) \tag{16}$$

$$\Psi_0^+(\boldsymbol{F}) = \frac{1}{2}\, \kappa \log^2(J^+) + \frac{1}{2}\, G \left[\operatorname{tr}(\boldsymbol{C}^{\mathrm{iso}}) - 3 \right] \qquad \text{with } J^+ := \max(\det \boldsymbol{F}, 1) \tag{17}$$

$$\Psi_0^-(\boldsymbol{F}) = \frac{1}{2} \kappa \log^2(J^-) \qquad \text{with } J^- := \min(\det \boldsymbol{F}, 1). \tag{18}$$

Computing the first-order optimality conditions of the minimization problem (14) and introducing the history variable $\mathcal{H} = \max\left(\mathcal{H}_n, \Psi_0^+\right)$ into these optimality conditions in order to fulfill thermodynamic consistency, leads to the balance equations for the displacement field $\boldsymbol{u}$ and phase-field variable d in local form

$$\operatorname{Div} \boldsymbol{P} = \boldsymbol{0} \tag{19}$$

$$\frac{g_c}{l} [d - l^2 \Delta d] + \eta\, \dot{d} = 2\,[1-d]\, \mathcal{H} \tag{20}$$

along with the Neumann boundary conditions

$$\boldsymbol{P} \cdot \boldsymbol{N} = \bar{\boldsymbol{T}} = \boldsymbol{0} \quad \text{and} \quad \nabla d \cdot \boldsymbol{N} = 0 \quad \text{on } \partial\Omega, \tag{21}$$

where $\boldsymbol{N}$ is the outward normal on $\partial\Omega$.

3 | IMPLENTATIONAL DETAILS

In this section, some details regarding the numerical implementation of the two-field problem are given. The displacement field $\boldsymbol{u}$ is obtained by solving balance of linear momentum for the bulks (19) and the interfaces (9). Within the ferrite grains, the crystal plasticity problem (8) is solved whereas the martensite is assumed to be elastic. The phase-field variable d is computed by solving balance equation (20) within the martensite grains only. These balance equations are then discretized and solved by standard finite-element approaches [15].

One important aspect to highlight is the staggered solution scheme. Solving for the displacement field $\boldsymbol{u}$ and the phase-field d in a monolithic fashion is challenging due to the nonconvexity of the underlying potential. Therefore, the subproblems for $\boldsymbol{u}$ and d are solved in an alternating manner until the combined residual $R = ||\,[\boldsymbol{R}^{\boldsymbol{u}}, \boldsymbol{R}^d]\,||$ is smaller than a desired tolerance. This scheme is proven to be very robust in practice and exhibits quadratic convergence in each subproblem [9].

Finally, the described models and algorithms are implemented into the finite element analysis program FEAP [16] as user elements where open source software DEIP [17] was used to place interface elements between the grains of the polycrystal.

TABLE 1 Constitutive parameters for ferrite and martensite.

	Bulk modulus κ in GPa	Shear moduls G in GPa	Initial yield limit Q_0^α in GPa	Hardening parameter ΔQ in GPa	Shape parameter p [−]
Ferrite	175	80.77	0.15	0.08	10
Martensite	175	80.77	—	—	—

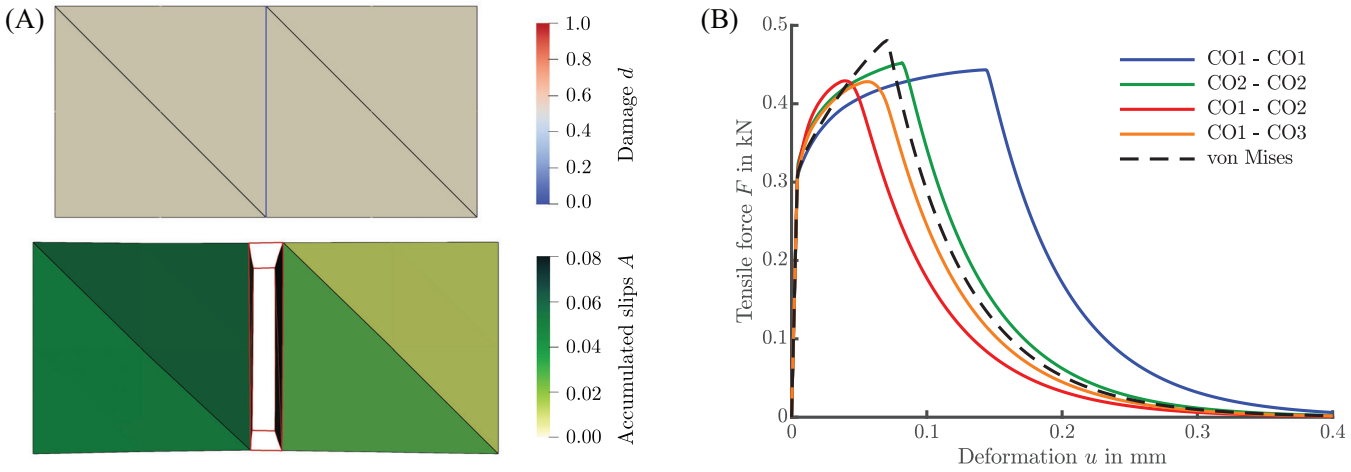

FIGURE 1 (A) Top: Initial geometry of two cubic ferrite grains ($1 \times 1 \times 1$ mm) with two different crystal orientations and an interface in-between. Bottom: Deformed state with fully damaged interfaces after applying a tensile deformation u. (B) Resulting force–displacement diagram for different combinations of crystal orientations (COX) of the two bulks. Additionally, the results computed by means of a von Mises plasticity are included.

4 | NUMERICAL EXAMPLES

In this section, two examples are presented to showcase the interaction of the mechanisms presented in Section 2. The first example highlights the interaction of the crystal plasticity formulation with the interface model and its effect on grain boundary decohesion. The second example features the cracking of a martensite band where all three mechanisms are included, that is, a crystal plasticity model for the ferrite grains, a phase-field model for the martensite and cohesive interfaces to capture grain boundary decohesion at grain boundaries.

In the simulations, the material parameters of the ferrite and martensite grains are inspired by microscopic DP800 experiments [18, 19], see Table 1. The damage-related parameters for the interfaces and the phase-field model are chosen such that the desired mechanisms are triggered in order to highlight the predictive capabilities of the presented framework.

4.1 | Grain boundary decohesion—interaction of crystal plasticity and interfaces

In order to investigate the impact of the crystal orientation of two adjacent ferrite grains on the corresponding grain boundary decohesion, a simple tensile test setting is chosen where an interface is placed between two cubic ferrites, as depicted in Figure 1A. A tensile test is conducted for different crystal orientations within the two bulks, where all other material parameters are kept constant.

From the force–displacement diagram in Figure 1B, it is obvious that the crystal orientation has a significant influence on the effective response. When both ferrites have the same crystal orientation (blue or green curve), pronounced plastic deformations occur before the interfaces damage. On the contrary, if the crystal orientations are very different (red or orange curve), less plastic deformations are observed and the interfaces crack earlier. This is in good agreement with experimental observations [20]. If the crystal plasticity model is replaced by a standard von Mises plasticity (black curve), this effect cannot be captured appropriately.

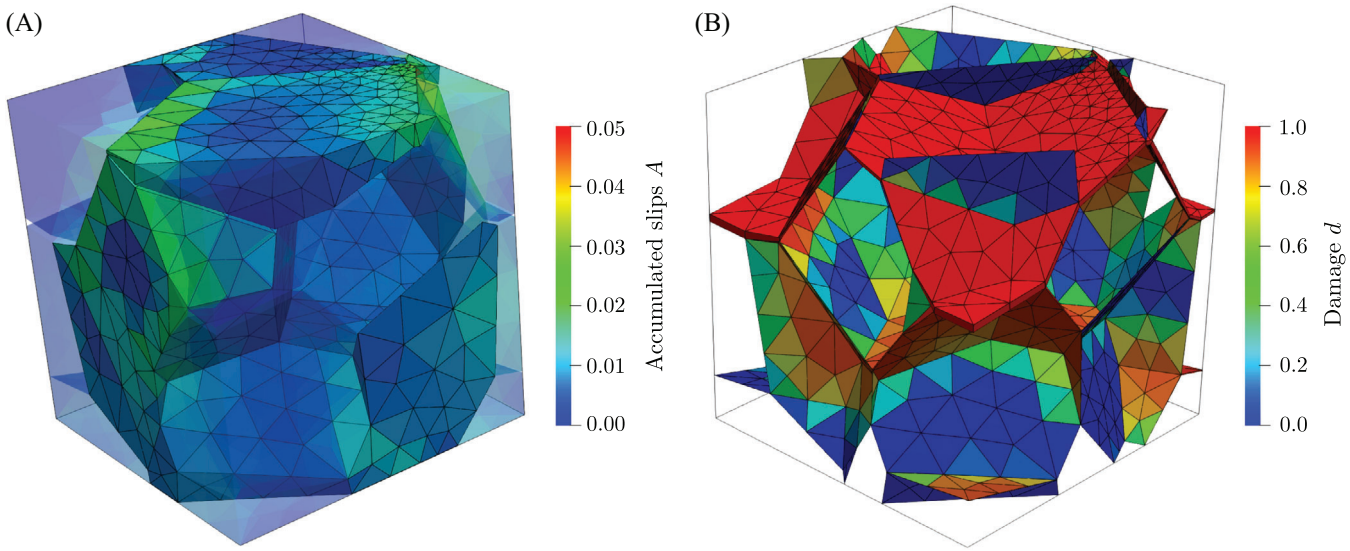

FIGURE 2 Simulation results of a periodic RVE consisting of six ferrite grains separated by interfaces elements where the strain path measured in a Nakajima test is prescribed. (A) Accumulated plastic slips A within the grains and (B) damage d at the interfaces are shown.

To showcase the interaction in a more complex setting, a 3D microstructure consisting of six ferrite grains with interface elements in-between is considered next, see Figure 2. For the ferrite grains, the crystal plasticity model of Section 2.1 is used where each grain has the same material parameters except for the crystal orientation, which is varied. All interface elements pose the same material parameters. The applied load path corresponds to a Nakajima test on DP800 [21], which is similar to bi-axial tension.

As expected, the plastic deformations accumulate near the grain boundaries, see Figure 2A. The intergranular crack path (Figure 2B) follows the grain boundaries and forms one continuous crack surface along the boundaries until the body is fully cracked, which is also in good agreement with the experimental observations [21].

4.2 | Cracking of a martensite band—interaction of all three mechanisms

The second example includes all three mechanisms presented in Section 2 in one RVE simulation. The considered periodic microstructure consists of a martensite band surrounded by two ferrite grains characterized by different crystal orientations, as depicted in Figure 3. Applying a tensile load in vertical direction leads to grain boundary decohesion at MF interfaces (Figure 3B). Conversely, a tensile load in horizontal direction leads to the opening of FF interfaces first (Figure 3C) which then initiates the cracking of the martensite band (Figure 3D). Triggering the martensite crack first is more challenging in this setting since it requires a stress singularity, which is also very sensitive w.r.t the properties of the interface elements.

5 | CONCLUSION

A framework that can capture the main (damage) mechanisms observed in DP steels at the microscale, that is, large plastic deformations within ferrite grains, grain boundary decohesion at FF and MF interfaces, as well as cracking of quasi-brittle martensite phases was proposed. This framework is based on a crystal plasticity model coupled with cohesive interfaces and a phase-field formulation. It can be used to investigate the interaction of aforementioned different mechanisms and, in turn, might help to understand void nucleation, growth, and coalescence DP steels. Furthermore, the framework may also be used to account for cracking or decohesion of inclusions or precipitates. In the future, a thorough calibration of the model based on microscale experiments of DP800 will be conducted and the framework will be employed to optimize loading path of forming processes.

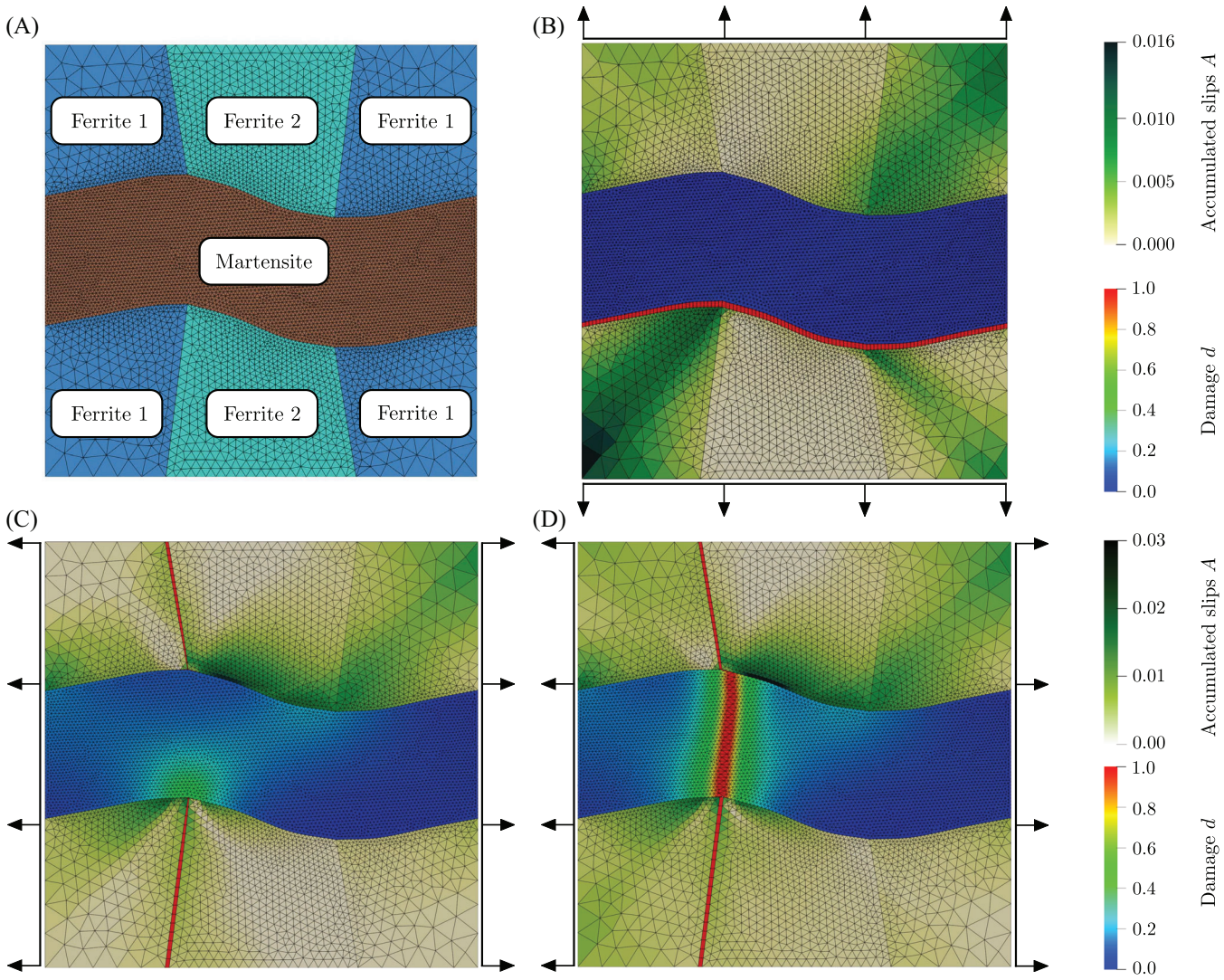

FIGURE 3 (A) Geometry of a martensite band embedded in a ferrite matrix. (B) Resulting grain boundary decohesion at martensite-ferrite interfaces after applying a tensile load in vertical direction. (C) and (D) Results after applying a tensile load in horizontal direction at two distinct time steps. Instance (C) showcases a time step where the ferrite–ferrite interfaces are already fully damaged but the martensite band is still intact. In the next time step, the martensite band breaks as shown in (D).

ACKNOWLEDGMENTS

Financial support from the German Research Foundation (DFG) via SFB/TRR 188 (project number 278868966), project C04, is gratefully acknowledged.

Open access funding enabled and organized by Projekt DEAL.

ORCID

Alexander Niehüser https://orcid.org/0009-0004-3412-130X
Jörn Mosler https://orcid.org/0000-0002-5797-0919

REFERENCES

1. Tasan, C., Diehl, M., Yan, D., Bechtold, M., Roters, F., Schemmann, L., Zheng, C., Peranio, N., Ponge, D., Koyama, M., Tsuzaki, K., & Raabe, D. (2015). An overview of dual-phase steels: Advances in microstructure-oriented processing and micromechanically guided design. *Annual Review of Materials Research*, *45*(1), 391–431.
2. Meya, R., Kusche, C., Löbbe, C., Al-Samman, T., Korte-Kerzel, S., & Tekkaya, A. (2019). Global and high-resolution damage quantification in dual-phase steel bending samples with varying stress states. *Metals*, *9*(3), 319.

3. Tian, C., Kusche, C. F., Medina, A., Lee, S., Wollenweber, M. A., Pippan, R., Korte-Kerzel, S., & Kirchlechner, C. (2024). Understanding the damage initiation and growth mechanisms of two DP800 dual phase grades. *Materials and Design*, *238*, 112630.
4. Asaro, R. J. (1983). Crystal plasticity. *Journal of Applied Mechanics*, *50*(4b), 921–934.
5. Schmidt-Baldassari, M. (2003). Numerical concepts for rate-independent single crystal plasticity. *Computer Methods in Applied Mechanics and Engineering*, *192*(11-12), 1261–1280.
6. Mosler, J., & Scheider, I. (2011). A thermodynamically and variationally consistent class of damage-type cohesive models. *Journal of the Mechanics and Physics of Solids*, *59*(8), 1647–1668.
7. Heitbreder, T., Ottosen, N. S., Ristinmaa, M., & Mosler, J. (2018). On damage modeling of material interfaces: Numerical implementation and computational homogenization. *Computer Methods in Applied Mechanics and Engineering*, *337*, 1–27.
8. Bourdin, B., Francfort, G., & Marigo, J. J. (2000). Numerical experiments in revisited brittle fracture. *Journal of the Mechanics and Physics of Solids*, *48*(4), 797–826.
9. Miehe, C., Hofacker, M., & Welschinger, F. (2010). A phase field model for rate-independent crack propagation: Robust algorithmic implementation based on operator splits. *Computer Methods in Applied Mechanics and Engineering*, *199*(45-48), 2765–2778.
10. Coleman, B. D., & Gurtin, M. E. (1967). Thermodynamics with internal state variables. *The Journal of Chemical Physics*, *47*(2), 597–613.
11. Anand, L., & Kothari, M. (1996). A computational procedure for rate-independent crystal plasticity. *Journal of the Mechanics and Physics of Solids*, *44*(4), 525–558.
12. Niehüser, A., & Mosler, J. (2023). Numerically efficient and robust interior-point algorithm for finite strain rate-independent crystal plasticity. *Computer Methods in Applied Mechanics and Engineering*, *416*, 116392.
13. Ottosen, N. S., Ristinmaa, M., & Mosler, J. (2016). Framework for non-coherent interface models at finite displacement jumps and finite strains. *Journal of the Mechanics and Physics of Solids*, *90*, 124–141.
14. Javili, A., Steinmann, P., & Mosler, J. (2017). Micro-to-macro transition accounting for general imperfect interfaces. *Computer Methods in Applied Mechanics and Engineering*, *317*, 274–317.
15. Zienkiewicz, O. C., Taylor, R. L., & Zhu, J. Z. (2005). *The finite element method: Its basis and fundamentals* (6th ed.). Elsevier Butterworth-Heinemann.
16. Taylor, R. L. (2020). *FEAP—finite element analysis programm*.
17. Truster, T. (2022). *DEIP—discontinuous element insertion program*.
18. Tian, C., Dehm, G., & Kirchlechner, C. (2021). Influence of strain rate on the activation of {110}, {112}, {123} slip in ferrite of DP800. *Materials*, *15*, 100983.
19. Tian, C., & Kirchlechner, C. (2021). The fracture toughness of martensite islands in dual-phase DP800 steel. *Journal of Materials Research*, *36*(12), 2495–2504.
20. Choi, S. H., Kim, E. Y., Woo, W., Han, S., & Kwak, J. (2013). The effect of crystallographic orientation on the micromechanical deformation and failure behaviors of DP980 steel during uniaxial tension. *International Journal of Plasticity*, *45*, 85–102.
21. Bergs, T., Nick, M., Trauth, D., & Klocke, F. (2018). Damage evolution in Nakajima tests of DP800 dual phase steel. *IOP Conference Series: Materials Science and Engineering*, *418*, 012048.

How to cite this article: Niehüser, A., & Mosler, J. (2024). Microscale modeling of damage mechanisms in dual-phase steel DP800. *Proceedings in Applied Mathematics and Mechanics*, *24*, e202400012. https://doi.org/10.1002/pamm.202400012